communications earth & environment

Article

A Nature Portfolio journal

https://doi.org/10.1038/s43247-026-03917-x

# The significance of water vapor isotopes in improving weather prediction

Check for updates

Kinya Toride[1,2,3], Kei Yoshimura[3], Matthias Schneider[4], Christopher Diekmann[4,5], Farahnaz Khosrawi[4,6], Benjamin Ertl[4,7] & Hayoung Bong[8]

Water vapor isotopes carry the integrated history of evaporation, condensation, mixing, and transport. Although previous studies have shown potential to improve forecasts under controlled conditions, real-world applications have been limited by systematic biases in both models and satellite retrievals arising from sparse measurements in the free troposphere. Here we assimilate mid-tropospheric δD retrievals (peak sensitivity ~4.2 km) from the Infrared Atmospheric Sounding Interferometer into the Isotope-incorporated Global Spectral Model and evaluate the added value beyond co-assimilated temperature and specific humidity with identical spatial and temporal coverage. Assimilating δD improves 0–120 h forecasts of wind, temperature, specific humidity, and geopotential height, with the largest gains in the midlatitudes; heavy-precipitation skill also increases for thresholds >3 mm per 6 h. Demonstrated in a coarse-resolution configuration with limited observations, the results indicate that isotopic information strengthens transport tracking and hydrological constraints, motivating evaluation in operational high-resolution forecasting systems.

The release and absorption of latent heat during water phase changes, such as condensation and evaporation, serve as the primary energy source for atmospheric circulation. However, accurately constraining this energy source remains a significant challenge. While global reanalysis datasets provide high-quality estimates of state variables like temperature and pressure, they often exhibit biases and inconsistencies in vertical heating structure and convective activity[1–4]. This discrepancy arises because vertical heating cannot be directly measured by current satellite or radiosonde networks; instead, models must infer it through complex physical parameterizations. These biases can degrade the accuracy of weather prediction, as the vertical heating profile plays a key role in large-scale circulation, wave propagation, storm track positioning, cloud development, and precipitation patterns[5–7]. On climate time scales, variations in convective processes significantly impact cloud feedback, radiative balance, and ultimately, climate sensitivity and projections of future climate changes[8,9].

Stable water isotopes (e.g., HDO and $H_2^{18}O$) provide a direct physical link to the latent heating processes through isotopic fractionation[10]. For instance, heavier isotopes preferentially condense into the liquid phase because of their greater binding energy and lower diffusive velocity. While traditional isotopic observations were primarily restricted to surface precipitation using mass spectrometers[11–13], advancements in satellite remote sensing have provided global coverage of vapor isotopic observations in the troposphere and stratosphere[14–17]. Most recently, the Infrared Atmospheric Sounding Interferometer (IASI) on the Meteorological Operational satellite program (MetOp) has provided long-term isotopic observations with high accuracy and spatiotemporal resolution in the mid-troposphere[18–21].

Due to their unique characteristics, isotopic observations can serve as additional constraints on the atmospheric heating structure and have the potential to improve weather prediction by enhancing the representation of latent heat release and vertical moisture distribution in numerical models[22,23]. However, the assimilation of satellite-observed water vapor isotopes has been confined to controlled conditions, either within a perfect model framework[22,24] or without assimilating other variables[25]. One of the major reasons for this limitation is inconsistency between remote-sensing observations and model simulations of vapor isotopes in the free troposphere due to the lack of sufficient in situ measurements for absolute calibration[26–28].

In this study, we demonstrate that assimilating IASI water vapor isotopic ratio (δD, relative to the Vienna Standard Mean Ocean Water)

[1]Cooperative Institute for Research in Environmental Sciences, University of Colorado Boulder, Boulder, CO, USA. [2]Physical Sciences Laboratory, National Oceanic and Atmospheric Administration, Boulder, CO, USA. [3]Institute of Industrial Science, University of Tokyo, Chiba, Japan. [4]Institute of Meteorology and Climate Research, Karlsruhe Institute of Technology, Karlsruhe, Germany. [5]Remote Sensing Products Division, European Organisation for the Exploitation of Meteorological Satellites, Darmstadt, Germany. [6]Jülich Supercomputing Centre, Forschungszentrum Jülich, Jülich, Germany. [7]Scientific Computing Center, Karlsruhe Institute of Technology, Karlsruhe, Germany. [8]NASA Postdoctoral Program Fellow, NASA Goddard Institute for Space Studies, New York, NY, USA.
e-mail: kinya.toride@noaa.gov

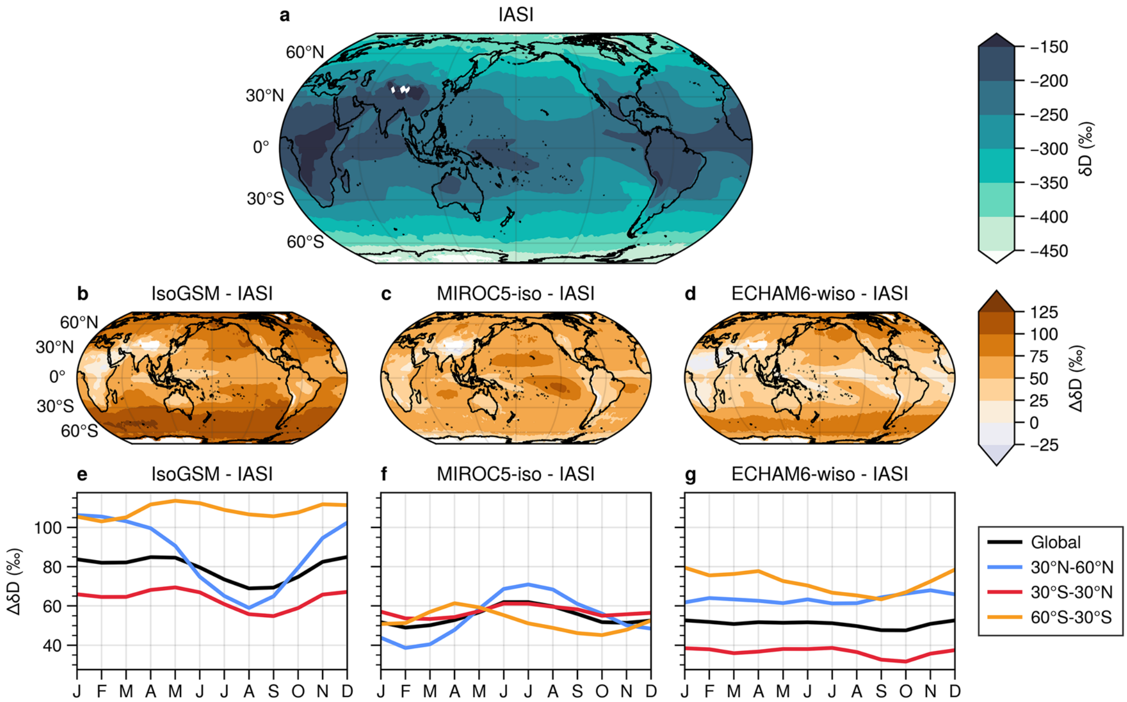


**Fig. 1 | Comparison of climatological mean δD between IASI observations and nudged model simulation.** **a** Spatial pattern of IASI δD super-observations (‰), with peak sensitivity near 4.2 km altitude, averaged from October 2014 to June 2019. **b**–**d** Mean δD differences between IASI observations and nudged simulations from three isotope-enabled models: **b** IsoGSM, **c** MIROC5-iso, and **d** ECHAM6-wiso. Differences in monthly mean δD (‰) averaged over the globe, 60°S–30°S, 30°S–30°N, and 30°N–60°N between IASI observations and nudged model simulations using **e** IsoGSM, **f** MIROC5-iso, and **g** ECHAM6-wiso. Positive values indicate higher δD in the model relative to IASI. All simulations are nudged toward JRA55, and IASI averaging kernels are applied to the collocated nudged simulations.

significantly improves atmospheric analysis and short-range forecasts, including precipitation. To address systematic offsets of δD relative to the model climatology, we apply a simple bias correction using 4.5 years of IASI observations to ensure filter stability. Our objective is to quantify the added value of δD assimilation beyond temperature and specific humidity observations with identical spatial and temporal coverage (Supplementary Fig. 1). This ensures that improvements result from complementary isotopic information rather than observational coverage differences. We employ the Isotope-incorporated Global Spectral Model (IsoGSM; T62 horizontal resolution, 28 vertical levels), following the established configuration in which IsoGSM behavior has been widely used and validated for water isotope applications[15,26,29,30]. Data assimilation is performed with the local ensemble transform Kalman filter (LETKF)[31], assimilating IASI observations with peak sensitivity in the mid-troposphere (~4.2 km). We acknowledge that T62 is coarse, resolving only synoptic-scale features and exhibiting smoother small-scale variability than modern operational systems. It also assimilates fewer observations than operational numerical weather prediction systems. Accordingly, our goal is not to reproduce operational performance, but to provide a controlled and computationally tractable framework for isolating the specific contribution of δD assimilation.

## Results

### Characterization and correction of systematic biases in δD prior to data assimilation

IASI δD retrievals exhibit significant offsets in climatology compared to the nudged model simulations using three isotope-enabled global circulation models (GCMs) (Fig. 1). This comparison is made with the IASI averaging kernels (highest sensitivity near 4.2 km altitude) and is restricted to clear-sky conditions to align with the sensitivity of the IASI retrievals. Generally, IASI δD exhibits typical “latitude effects,” with values decreasing from approximately −200‰ in the tropics to −450‰ in the polar regions (Fig. 1a). This gradient reflects the progressive depletion of heavier isotopes due to condensation processes as air masses move poleward[32,33]. While all three models reproduce the general latitudinal pattern, they tend to simulate higher δD values than those retrieved from IASI, though part of this discrepancy may also reflect uncertainties or biases in the satellite observations. IsoGSM and ECHAM6-wiso exhibit smaller differences in the tropics (up to 75‰) and larger differences at higher latitudes (up to 125‰), leading to reduced latitudinal gradients (Fig. 1b, d). In contrast, MIROC5-iso shows a relatively uniform difference of about 50‰ across all latitudes (Fig. 1c).

The differences between IASI and the models exhibit distinct seasonality (Fig. 1e–g). IsoGSM shows higher seasonal dependency in the Northern Hemisphere and larger differences during winter. MIROC5-iso also displays higher seasonal dependency in the Northern Hemisphere, but larger differences are observed during summer. ECHAM6-wiso, on the other hand, tends to show relatively constant differences across seasons, with greater seasonal variability observed in the Southern Hemisphere. It should be noted that these differences depend on the observational frequency of IASI, which observes δD more frequently in the summer hemisphere (Supplementary Fig. 2).

The observational and model contributions to the systematic δD differences cannot be directly compared, as they stem from different sources. Satellite δD retrievals carry uncertainties from spectroscopy, vertical sensitivity, and sampling[18–21], while isotope-enabled GCMs contain structural uncertainties in convection, microphysics, and mixing[26,34,35]. Both can produce climatological offsets of several tens of ‰, making it plausible that each contributes to the discrepancies found in Fig.1. For these reasons, systematic differences between satellite retrievals and models vary depending on which observation and model are compared and could even change the sign[26–28].

A systematic model bias may arise from the long-standing use of precipitation isotopes to guide model development[29,36–40]. Because precipitation isotopes integrate the full history of condensation, mixing, and sub-cloud processes, tuning or validating models against precipitation does not necessarily constrain the processes that govern free-tropospheric

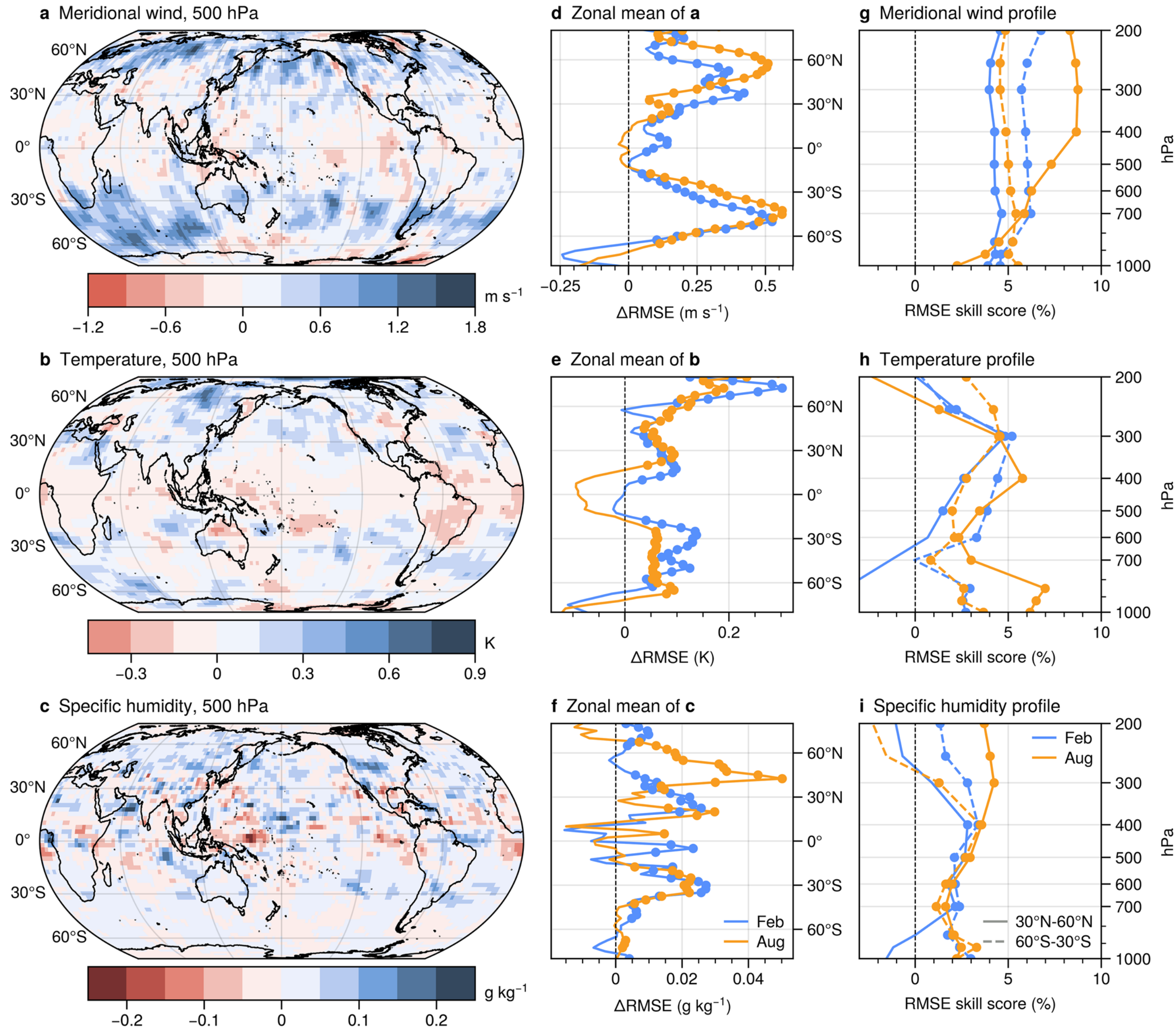


**Fig. 2 | Improvements by IASI δD assimilation.** **a**–**c** Spatial patterns of RMSE reduction by δD assimilation for **a** meridional wind (m s$^{-1}$), **b** temperature (K), and **c** specific humidity (g kg$^{-1}$) at 500 hPa during August 2017. Positive values indicate improvements in RMSE due to δD assimilation. **d**–**f** Corresponding zonal mean RMSE reductions during February and August 2017. **g**–**i** Vertical profiles of RMSE skill score (%) in the midlatitudes during February and August 2017. Dots denote statistically significant improvements at the 5% level.

isotopes[27,35]. As a result, parameterizations that have little effect on precipitation isotopes, such as convective detrainment, rain re-evaporation, or mixing, could lead to systematic biases in tropospheric δD. Finally, nudging is unlikely to be the primary cause since the three models show different spatial and seasonal bias patterns, and δD biases often appear even in free-running isotope GCM simulations[27].

In the context of data assimilation, these systematic biases obscure physically meaningful isotopic signals for improving weather prediction and can lead to instability in the analysis cycle, including filter divergence. Here, we remove these seasonally and spatially varying biases and assimilate bias-corrected δD using IsoGSM. The same bias removal process is applied to specific humidity and temperature observations for consistency.

### Improvement of 3D atmospheric analysis by isotopic constraints

To quantify the impact of water isotopes, we compare a baseline experiment assimilating only temperature ($T$) and specific humidity ($q$) against an experiment that additionally assimilates δD. As shown in Fig. 2, the assimilation of δD reduces the root-mean-squared error (RMSE) across key prognostic state variables when evaluated against the European Centre for Medium-Range Weather Forecasts (ECMWF) reanalysis v5 (ERA5). To provide the absolute error context for these relative improvements, Supplementary Figs. 3 and 4 show the global RMSEs of these experiments and the corresponding free forecast. Notable improvements are observed in meridional wind at 500 hPa over midlatitude storm track regions, where extratropical cyclones preferentially travel (Fig. 2a). These improvements also extend to the assimilated variables (i.e., temperature and specific humidity), particularly in the midlatitudes (Fig. 2b, c), demonstrating the added value of δD assimilation.

Consistent improvements in the midlatitudes are observed in both the February and August experiments, while almost no improvements are seen in the tropics across all the variables (Fig. 2d–f). The most significant improvements in meridional wind in the Northern Hemisphere shift from around 35°N in February to around 60°N in August, likely tied to changes in jet streams and observational distributions. Conversely, improvements in the Southern Hemisphere remain unchanged across both seasons. The temperature improvement pattern is relatively similar in both seasons, with the largest improvements occurring in the northern polar region. Specific humidity shows more localized impacts, with the largest impacts shifting northward in the Northern Hemisphere in August, similar to the meridional wind results.

The small impacts in the tropics contradict the findings of perfect model experiments[22]. Despite the observations of super Rayleigh signals linked to tropical convective activity in IASI δD data[41], this indicates that simply eliminating climatological bias is insufficient for assimilating real observational data in the tropics. In fact, observed δD variability is lower than modeled variability in this region (Supplementary Fig. 5), and correlation coefficients between IASI and nudged simulations are reduced as well (Supplementary Fig. 6). This discrepancy may be due to the IASI's limited ability to accurately observe δD in cloudy areas and limitations in model physics to resolve tropical convective processes.

The assimilation impacts of mid-tropospheric vapor isotopes in the midlatitudes permeate the entire troposphere (Fig. 2g–i). The impacts on wind fields exhibit a relatively uniform distribution with height, yielding about 5% improvements on average. In contrast, improvements in temperature and specific humidity are larger in the lower and upper troposphere compared to the middle troposphere (500–700 hPa), where these observations are assimilated. These non-local impacts of δD assimilation are supported by the upwelling motion of convective activity where phase changes occur[22]. Overall, improvements are more significant in the summer hemisphere, which could be related to greater observational coverage due to better sensitivity in humid conditions (Supplementary Fig. 2) and higher variability in observed δD relative to modeled δD (Supplementary Fig. 7). The model-observation difference in variability may be attributed to the higher spatial resolution of IASI and the model's tendency to more closely follow Rayleigh fractionation curves[20].

### Improvement of short-term weather forecasts

Improvements in the analysis fields (i.e., initial conditions used for forecasting) lead to improvements in short-term weather forecasts (Fig. 3). While skill improvements decrease with forecast lead time, the positive effects of δD assimilation greatly outweigh the negative effects. For wind speed, improvements are more pronounced in the upper troposphere and can persist beyond 120 h, especially in the summer hemisphere. A similar trend is observed for temperature and specific humidity forecasts, with reduced impacts due to the assimilation of these variables. Interestingly, geopotential height, a vital field for understanding the structure of weather systems, shows more than 10% improvements. This could be attributed to reductions in mean error, particularly observed in the geopotential height field (Supplementary Figs. 8, 9).

These forecast improvements are evident even when evaluated globally (Supplementary Fig. 10), highlighting the overall positive impacts of δD assimilation. Wind speed and geopotential height forecasts show significant improvements throughout the troposphere, while temperature and specific humidity forecasts are particularly improved in the mid to upper troposphere. These results demonstrate potential benefits of global weather prediction by the integration of δD assimilation.

### Improved forecast skills for heavy precipitation and attribution analysis

While atmospheric analysis and forecast fields are evaluated using ERA5, short-term precipitation forecasts are assessed using the Integrated Multi-satellite Retrievals for Global Precipitation Measurement (IMERG), a satellite-based precipitation dataset. This analysis aims to ensure that the improvements observed with ERA5, which does not assimilate isotopic observations, are also detectable using an independent satellite observation dataset.

Positive impacts on precipitation forecast are observed for events with intensities greater than 3 mm per 6 h in the midlatitudes (Fig. 4a, b). In contrast, forecasts for weaker precipitation tend to have little to no impact or negative impacts. The improvements are more pronounced for extreme precipitation events, which are associated with stronger latent heating and clearer isotopic signatures. In the tropics, while more negative impacts are observed, some positive impacts are still evident for extreme precipitation events in both February and August. This indicates that, despite larger model-observation biases in the tropics, the strong signal-to-noise ratio from extreme convective activities can compensate for these limitations.

The influence of water vapor isotopes arises from both dynamic processes (transport and mixing) and thermodynamic processes (local phase change). To isolate these effects, we conduct additional experiments using the variable localization method[22,42], which restricts the direct impact of δD assimilation to specific prognostic variables. In the Dynamic experiment, δD observations are excluded from the LETKF weight calculation for specific humidity and temperature, restricting their direct analysis impact to the wind fields. Conversely, in the Thermodynamic experiment, δD assimilation is prevented from influencing zonal and meridional wind (see "Methods" for details). Because δD is a passive tracer, any impacts on winds, temperature, or humidity arise from multivariate analysis increment and subsequent forecast adjustments, not from direct model-physics feedback.

Overall, the Dynamic experiment yields greater improvements than the Thermodynamic experiment in both seasons (Fig. 4c–f). Although this is partly expected as wind fields are not directly assimilated, it highlights that δD holds unique information about atmospheric transport beyond what is captured by water vapor alone. The Dynamic experiment even shows improved precipitation forecasts over the tropics in August as opposed to the full covariance experiment (cf. Fig. 4b, d), suggesting a potential issue in the model's δD-humidity relationship in the tropical region during this season. In contrast, the Thermodynamic experiment exhibits consistent improvements primarily in the summer hemisphere, where δD assimilation has the strongest impact on the analysis fields.

Interestingly, the February experiment reveals that the impacts of the two localization experiments do not simply sum to the improvements observed in the full covariance experiment. While the Northern Hemisphere shows greater improvements compared to the Southern Hemisphere under the full covariance configuration (Fig. 4a), this pattern is absent in both the Dynamic (Fig. 4c) and Thermodynamic (Fig. 4e) experiments. This discrepancy suggests that neither dynamic nor thermodynamic processes alone can fully explain the observed impacts. Instead, it implies that non-linear interactions between dynamic and thermodynamic processes are essential for improving precipitation forecasts in this region and season.

## Conclusions

Assimilating δD improves atmospheric analysis and short-term weather prediction globally, with the largest gains in the midlatitudes. Despite the presence of biases in models and retrievals, this study demonstrates that IASI δD effectively captures the spatiotemporal variability that supplements co-assimilated temperature and humidity observations with identical coverage. Together with recent advances in isotope-enabled cloud-resolving models[43–46], these results highlight opportunities to better diagnose moist processes, refine isotopic parameterizations, and strengthen evaluation of free-tropospheric measurements against in situ observations.

While our coarse T62L28 setup with limited observations isolates the isotopic signal, the findings may not translate directly to operational systems. Future work should evaluate δD assimilation in high-resolution models with a full observing system, including radiosonde, aircraft, and all-sky satellite observations. These tests will determine whether the synoptic-scale benefits identified here extend to modern systems and whether δD provides independent constraints on moisture transport and hydrological processes in operational environments.

## Methods

### MUSICA IASI isotopologue pair product

The MUlti-platform remote Sensing of Isotopologues for investigating the Cycle of Atmospheric water (MUSICA) Infrared Atmospheric Sounding Interferometer (IASI) water isotopologue pair product[21] is obtained from the Institute of Meteorology and Climate Research Atmospheric Trace Gases and Remote Sensing (https://www.imk-asf.kit.edu/english/musica-iasi-h2oiso-v2.php). This dataset provides global δD, specific humidity, and temperature retrievals twice per day (about 350,000 points each) from

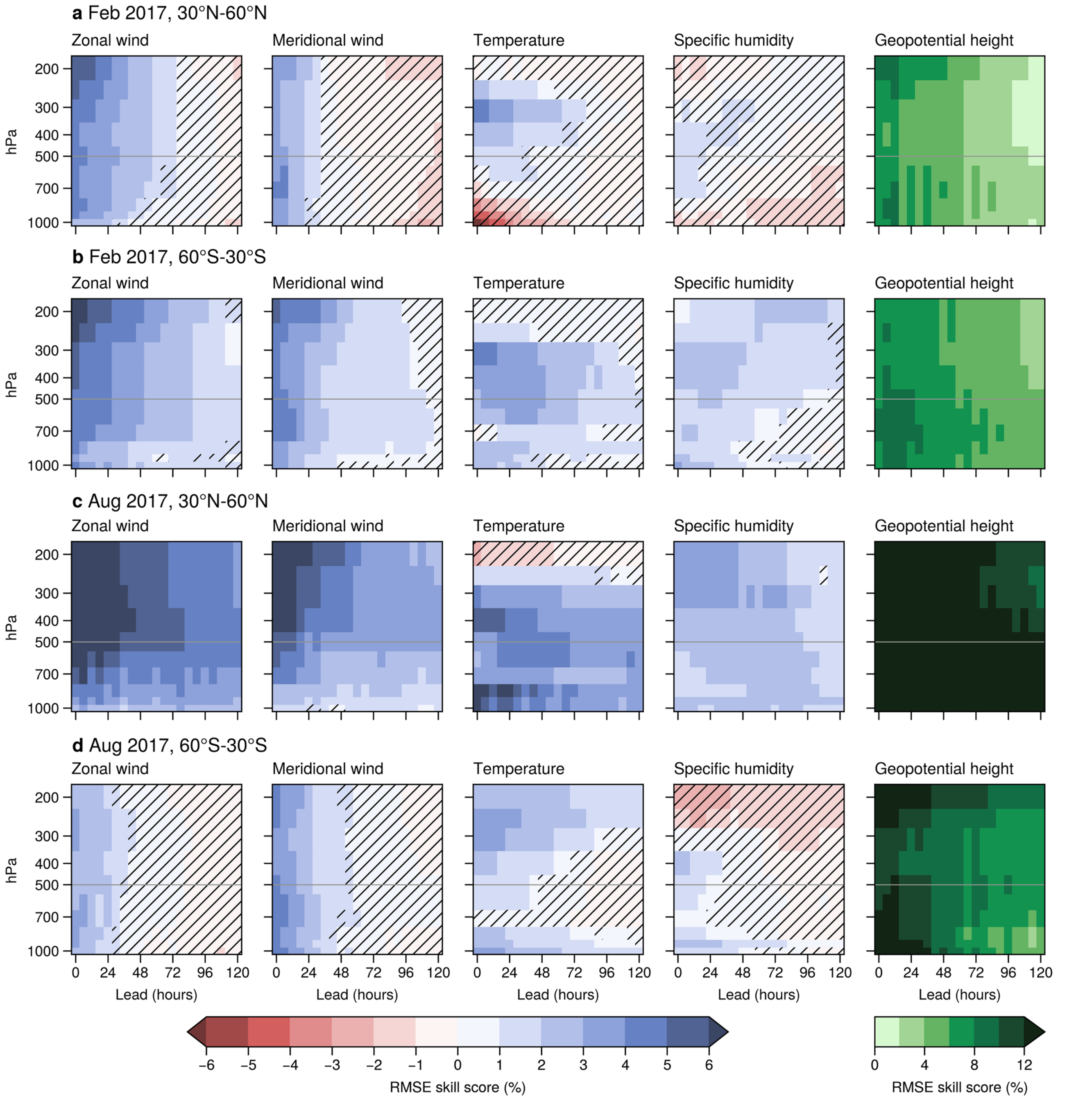


**Fig. 3 | Forecast improvements by IASI δD assimilation.** Vertical profiles of RMSE skill score (%) as a function of forecast lead time for zonal wind, meridional wind, temperature, specific humidity, and geopotential height for **a** 30°N–60°N during February 2017, **b** 60°S–30°S during February 2017, **c** 30°N–60°N during August 2017, and **d** 60°S–30°S during August 2017. Hatching indicates where the improvement is not statistically significant at the 5% level. Note that the color bar used for geopotential height differs from the others for display purposes.

October 2014 to June 2019, with vertical profile information in the free troposphere.

In this study, we focus on a single layer where the IASI retrievals exhibit maximum sensitivity, centered around 4.2 km altitude (atmospheric_levels = 19). To ensure data quality, we select retrievals with cloud-free or minor cloud cover (eumetsat_cloud_summary_flag = 1 or 2) and fair to good quality (musica_fit_quality_flag = 2 or 3). The selected retrievals are spatially and temporally aggregated to 6-h T62 grid cells (approximately 180 km) to match the model resolution. For each grid cell and 6-h window, we define the super-observation as the retrieval whose δD value is the median among all retrievals in that grid cell. The corresponding specific humidity, temperature, averaging kernels (vertical profiles of sensitivity), and a priori profiles (initial guess used in the retrieval) are taken from the same retrieval, rather than being independently averaged or median-aggregated across retrievals. Grid cells with fewer than 10 valid retrievals are excluded as a sampling-quality control, following previous satellite–model isotope comparison work[26]. An example of the super-observation generation procedure is shown in Supplementary Fig. 11. The temperature, water vapor, and δD a priori are based on atmospheric temperature from the European Organization for the Exploitation of Meteorological Satellites (EUMETSAT) Level-2 product, the climatological seasonal cycle of water vapor from Community Earth System Model version 1/Whole Atmosphere Community Climate Model (CESM1/WACCM) data, and an empirical relationship between

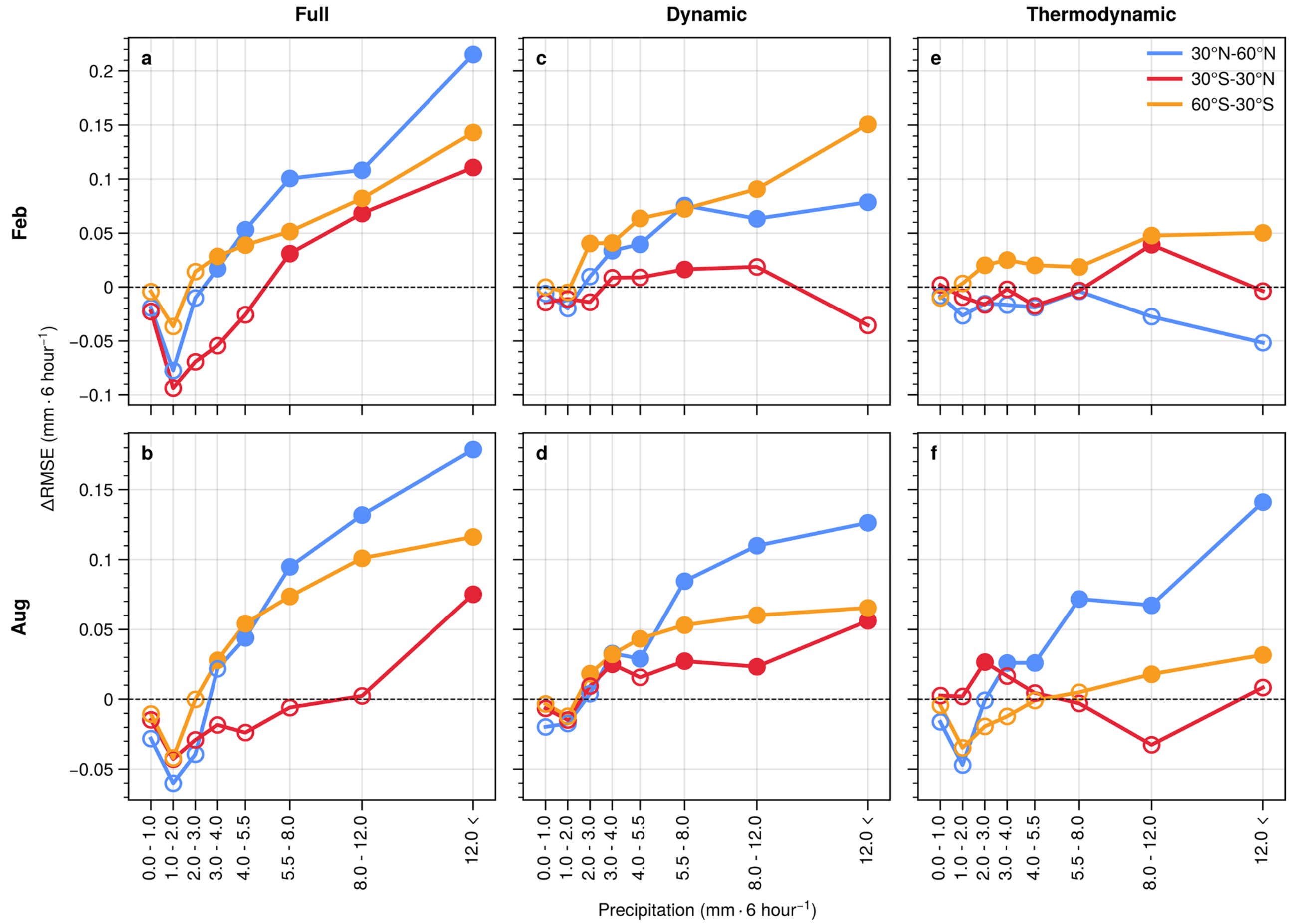


**Fig. 4 | Improvements in precipitation forecasts and decomposition of dynamical and thermodynamical contributions. a**, **b** RMSE reductions in 6-h precipitation forecasts (mm 6 h$^{-1}$) over 60°S–30°S, 30°S–30°N, and 30°N–60°N for **a** February and **b** August 2017. **c**, **d** Similar to (**a**, **b**) but for the Dynamic experiment (influence restricted to wind fields). **e**, **f** Similar to (**a**, **b**) but for the Thermodynamic experiment (influence restricted to q and T). Filled circles indicate statistically significant improvements at the 5% level. The IMERG precipitation dataset is used as a reference.

δD and water vapor derived from in situ measurements, respectively, as described in Schneider et al.[47].

The systematic biases between IASI and IsoGSM are estimated using a nudged simulation from October 2014 to June 2019, as described in the following section. Since biases can vary with season and geographical location, we estimate seasonally varying biases at each grid point. First, collocated IsoGSM outputs are vertically interpolated to the IASI coordinate at each grid point. The corresponding IASI averaging kernels and a priori are then applied to the interpolated modeled fields to derive vertically smoothed δD and specific humidity values with peak sensitivity around 4.2 km altitude. Next, we calculate the daily-mean bias at each grid point for each day of the year. A 5-day 15° × 15° running mean filter is then applied to smooth the biases. Missing values are filled by linear interpolation over time, and the bias climatology is further smoothed by taking the first four harmonics at each grid point. To remove data-sparse regions, we only use observations between 65°S and 65°N. This ensures that the missing values are fewer than 20 within 365 days (95% coverage in time). The bias climatology of temperature is similarly estimated without applying averaging kernels. The estimated bias climatology is added to the IASI observed values to ensure these values have no systematic biases in the model space during data assimilation.

The observation-error variance used for data assimilation is calculated as the sum of the instrumental error variance, the horizontal representativeness error variance, and an additional observation-error inflation term. The instrumental error is taken from the IASI retrieval product, whereas the horizontal representativeness error is estimated from the variance of retrievals within each 6-h T62 grid cell. The additional observation-error inflation term accounts for unresolved error components not represented by these diagnosed terms, particularly residual model–observation mismatch after mean bias correction, retrieval-smoothing, and a priori-related uncertainty associated with the averaging kernels, vertical and temporal representativeness error, and correlated retrieval errors. To maintain stable filtering, constant inflation standard deviations of 40‰ for δD and 0.6 g kg$^{-1}$ for specific humidity are applied. No additional inflation term is applied to temperature because temperature assimilation remained stable without it. Supplementary Fig. 12 shows an example of the spatial distributions of instrumental and horizontal representativeness errors. Over the full period, the time–space averaged instrumental and horizontal representativeness errors are 16.4‰ and 17.6‰ for δD, 0.23 and 0.38 g kg$^{-1}$ for specific humidity, and 1.0 and 0.69 K for temperature. The relatively large additional inflation terms suggest that residual state-dependent model–retrieval mismatch and retrieval-space mapping uncertainties remain in the innovations, particularly for the q–δD retrieval pair where averaging kernels and a priori information are applied.

### Nudged simulations using Isotope-enabled general circulation models

We use three nudged simulation datasets from isotope-enabled GCMs to demonstrate systematic biases between IASI and models[28]. The three GCMs include IsoGSM[29], MIROC5-iso[48], and ECHAM6-wiso[49]. These GCMs are nudged toward JRA55 every 6 h. Further details of the models and experimental design can be found in Bong et al.[28]. We use data from October 2014 to June 2019 and regrid all datasets to T62 horizontal resolution to enable consistent comparison with the IASI data. The climatological biases between IASI and each model are estimated using the method explained in the preceding section.

### Data assimilation

We assimilate IASI data using IsoGSM with the local ensemble transform Kalman filter (LETKF)[31]. Supplementary Fig. 1 shows the schematic overview of the data assimilation system. We use an IsoGSM version with a newly incorporated tracer transport scheme, named Non-iteration Dimensional-split Semi-Lagrangian (NDSL), which improves humidity and transport behaviors[50]. The model predicts water vapor isotopes as passive tracers, which do not alter temperature, moisture, momentum, or mass fields. The model runs on T62 horizontal resolution and 28 vertical sigma levels with 96 ensembles. The sea surface temperature and sea ice distribution used in the National Centers for Environmental Prediction/Department of Energy Reanalysis 2 (NCEP-DOE Reanalysis 2)[51] are used as lower boundary conditions.

LETKF updates the state estimate locally in a transformed space, offering significant advantages in computational efficiency and scalability compared to the traditional ensemble Kalman filter (EnKF). The state vector used in LETKF includes horizontal wind speeds, temperature, specific humidity, water isotope ratios (δD and $\delta^{18}$O), and surface pressure. The observations are assimilated every 6 h. Ensemble covariance is inflated by the relaxation to prior spread (RTPS) method[52] with the relaxation parameter of 0.95. The horizontal localization scale is selected to be 500 km (the influence radius of 1826 km). The ensemble size and localization scale follow our previous Observing System Simulation Experiment (OSSE) configuration[22], while the localization scale is additionally evaluated using sensitivity tests with 250, 500, and 750 km. Among the tested values, 500 km provides the best overall performance. The RTPS parameter and prescribed observation-error variances are selected through sensitivity experiments designed to maintain stable cycling throughout the assimilation period, particularly for q and δD assimilation. The RTPS value is larger than that used in the previous perfect-model OSSE (0.4) because real-observation cycling includes unresolved sources of model–observation mismatch that are absent from idealized experiments, including model error, representativeness error, retrieval-space uncertainty, and correlated retrieval errors. These errors are not fully represented by the prescribed diagonal observation-error covariance. Smaller observation-error variances or weaker relaxation result in systematic error growth, most notably in geopotential height, indicating overconfident analysis updates. Although further tuning may improve absolute forecast skill, the adopted settings provide a stable baseline, and the same configuration is used across experiments to evaluate the relative impact of δD assimilation.

Observation-space diagnostics over the evaluation period (Supplementary Figs. 13–15) show that the LETKF update reduces analysis departures relative to first-guess departures for T, q, and δD, while retaining finite ensemble spread after assimilation. The prescribed observation errors are generally larger than the diagnosed departure statistics, particularly for δD, indicating a conservative specification of observational uncertainty.

δD and specific humidity are assimilated using averaging kernels. Prior to assimilation, the mixing ratios of $H_2O$ and HDO simulated by IsoGSM are interpolated both horizontally and vertically to align with the location and vertical coordinate of an IASI observation. Subsequently, the corresponding averaging kernels and a priori are applied to transform the model state into the observation space. Finally, the model state vector is updated using bias-corrected IASI observations.

### Experimental design

We perform two data assimilation experiments to investigate the impacts of IASI δD. The control experiment, referred to as the "tq" experiment, assimilates only temperature and specific humidity observations from IASI. The second experiment, referred to as the "tqδD" experiment, additionally assimilates δD observations. These experiments are evaluated during two periods: February and August 2017, to assess δD impacts across different seasons.

For ensemble initialization, we first generate a long-term free run of the IsoGSM initialized at 0000 UTC June 1, 2015. The initial conditions for 96 ensemble members are selected from the free run from 0000 UTC January 1, 2017, and 0000 UTC July 1, 2017, with a 6-h time step for the February and August experiments, respectively. Observations are assimilated for 2 months, and the latter 1-month period is used for evaluation.

The effects of δD assimilation on short-term weather forecasts are assessed by conducting free ensemble forecasts from the analysis of each experiment. These forecasts are initialized every 2 days in February and August 2017 and simulated for a lead time of 120 h.

To isolate the impacts of thermodynamic and dynamic aspects of isotopic processes, we conduct sensitivity experiments using a cross-variable localization method[22,42] (Supplementary Table 1). These experiments assimilate the same observation types as the tqδD experiment, but modify the variable-localization factors used in the LETKF analysis. In our LETKF implementation, the analysis weights are computed separately for each target state variable using a local set of observations selected by horizontal, vertical, and variable localization. Setting a variable-localization factor to zero excludes the corresponding observation type from the weight calculation for that target variable. In the "Dynamic experiment," δD observations are excluded from the local LETKF weight calculation when updating thermodynamic variables ($q$ and $T$), thereby isolating the δD influence on the wind fields ($u$ and $v$). Conversely, in the "Thermodynamic experiment," δD observations are excluded when updating horizontal winds, thereby isolating the impact on the thermodynamic variables. These localizations are applied one-way; the variable-localization factors are modified only for the updates driven by δD observations, while the assimilation of temperature and humidity observations remains unchanged.

### Reference data

The European Center for Medium-Range Weather Forecasts (ECMWF) reanalysis v5 (ERA5)[53] is used as the ground truth for evaluating atmospheric fields. Although ERA5 does not assimilate water vapor isotopes, it is assumed to offer better accuracy due to its extensive assimilation of observations, advanced model physics, and higher spatiotemporal resolution. Atmospheric fields are evaluated using daily means, considering twice-daily observations by IASI.

To evaluate precipitation forecasts, we use the Global Precipitation Measurement (GPM) Integrated Multi-satellitE Retrievals for GPM (IMERG) version 06[54]. The IMERG algorithm integrates precipitation estimates from satellite passive microwave sensors to yield a global high-resolution (30 min and 0.1°) dataset. For the purpose of evaluating precipitation forecasts, we aggregate this data to a 6-h, T62 resolution using a conservative remapping technique.

### Evaluation

We evaluate the skill based on root-mean square error (RMSE) weighted by the area of grid cells. For skill scores, we use the RMSE skill score defined by $(\mathrm{RMSE_{CTRL}} - \mathrm{RMSE})/\mathrm{RMSE_{CTRL}}$, where $\mathrm{RMSE_{CTRL}}$ is the RMSE of the baseline control experiment.

The statistical significance of improvements by adding water isotopes is assessed using a one-sided permutation test (resampling without replacement) applied to the time series of paired experiments. For instance, if analysis or forecasts from the tqδD experiment are represented as $x = [x_1\ x_2\ x_3]$ and those from the tq experiment as $y = [y_1\ y_2\ y_3]$, these can be permuted to form new pairs, such as $x = [y_1\ x_2\ y_3]$ and $y = [x_1\ y_2\ x_3]$. The permutation is conducted along the time axis to preserve spatial structures. The null hypothesis is that true improvement is zero or negative, which is rejected at the significance level of 5%. The null distribution is constructed through 10,000 permutations, and the 95th percentile of this distribution is used as the threshold.

## Data availability

The MUSICA IASI water isotopologue pair product is available from the Institute of Meteorology and Climate Research Atmospheric Trace Gases and Remote Sensing (https://www.imk-asf.kit.edu/english/musica-iasi-h2oiso-v2.php) and referenced to https://doi.org/10.35097/415. ERA5 is available from the Copernicus Climate Change Service (C3S) Climate Data Store (https://doi.org/10.24381/cds.bd0915c6). IMERG precipitation data is available from the NASA Goddard Earth Sciences Data and Information Services Center (https://doi.org/10.5067/GPM/IMERG/3B-HH/06). IsoGSM, MIROC5-iso, ECHAM6-wiso nudged simulation datasets are available at https://doi.org/10.5281/zenodo.10624475. The experimental results that support the findings of this study are available at https://doi.org/10.7910/DVN/E28XJX.

Received: 17 July 2025; Accepted: 3 August 2026;
Published online: 03 September 2026

## References

1. Ling, J. & Zhang, C. Diabatic heating profiles in recent global reanalyses. *J. Clim.* **26**, 3307–3325 (2013).
2. Ren, P., Kim, D., Ahn, M.-S., Kang, D. & Ren, H.-L. Intercomparison of MJO column moist static energy and water vapor budget among six modern reanalysis products. *J. Clim.* **34**, 2977–3001 (2021).
3. Wolding, B. et al. Tropical thermodynamic–convection coupling in observations and reanalyses. *J. Atmos. Sci.* **79**, 1781–1803 (2022).
4. Serra, Y. L., Rutledge, S. A., Chudler, K. & Zhang, C. Rainfall and convection in ERA5 and MERRA-2 over the Northern Equatorial Western Pacific during PISTON. *J. Clim.* **36**, 845–863 (2023).
5. Hartmann, D. L., Hendon, H. H. & Houze, R. A. Some implications of the mesoscale circulations in tropical cloud clusters for large-scale dynamics and climate. *J. Atmos. Sci.* **41**, 113–121 (1984).
6. Branstator, G. Long-lived response of the midlatitude circulation and storm tracks to pulses of tropical heating. *J. Clim.* **27**, 8809–8826 (2014).
7. Toride, K. & Hakim, G. J. Influence of low-frequency PNA variability on MJO teleconnections to North American atmospheric river activity. *Geophys. Res. Lett*. **48**, e2021GL094078 (2021).
8. Bony, S. et al. Clouds, circulation and climate sensitivity. *Nat. Geosci.* **8**, 261–268 (2015).
9. Li, R. L., Studholme, J. H. P., Fedorov, A. V. & Storelvmo, T. Precipitation efficiency constraint on climate change. *Nat. Clim. Change* **12**, 642–648 (2022).
10. Galewsky, J. et al. Stable isotopes in atmospheric water vapor and applications to the hydrologic cycle. *Rev. Geophys.* **54**, 809–865 (2016).
11. Dansgaard, W. The abundance of $O^{18}$ in atmospheric water and water vapour. *Tellus* **5**, 461–469 (1953).
12. Dansgaard, W. Stable isotopes in precipitation. *Tellus* **16**, 436–468 (1964).
13. Craig, H. Isotopic variations in meteoric waters. *Science* **133**, 1702–1703 (1961).
14. Worden, J., Noone, D. & Bowman, K. Importance of rain evaporation and continental convection in the tropical water cycle. *Nature* **445**, 528–532 (2007).
15. Frankenberg, C. et al. Dynamic processes governing lower-tropospheric $HDO/H_2O$ ratios as observed from space and ground. *Science* **325**, 1374–1377 (2009).
16. Steinwagner, J. et al. Tropical dehydration processes constrained by the seasonality of stratospheric deuterated water. *Nat. Geosci.* **3**, 262–266 (2010).
17. Högberg, C. et al. The SPARC water vapour assessment II: profile-to-profile and climatological comparisons of stratospheric $\delta D(H_2O)$ observations from satellite. *Atmos. Chem. Phys.* **19**, 2497–2526 (2019).
18. Lacour, J.-L. et al. Mid-tropospheric δD observations from IASI/MetOp at high spatial and temporal resolution. *Atmos. Chem. Phys.* **12**, 10817–10832 (2012).
19. Schneider, M. et al. Accomplishments of the MUSICA project to provide accurate, long-term, global and high-resolution observations of tropospheric $\{H_2O, \delta D\}$ pairs—a review. *Atmos. Meas. Tech.* **9**, 2845–2875 (2016).
20. Schneider, M. et al. MUSICA MetOp/IASI $\{H_2O, \delta D\}$ pair retrieval simulations for validating tropospheric moisture pathways in atmospheric models. *Atmos. Meas. Tech.* **10**, 507–525 (2017).
21. Diekmann, C. J. et al. The global and multi-annual MUSICA IASI $\{H_2O, \delta D\}$ pair dataset. *Earth Syst. Sci. Data* **13**, 5273–5292 (2021).
22. Toride, K. et al. Potential of mid-tropospheric water vapor isotopes to improve large-scale circulation and weather predictability. *Geophys. Res. Lett.* **48**, 1–10 (2021).
23. Schneider, M. et al. Assessing the potential of free-tropospheric water vapour isotopologue satellite observations for improving the analyses of convective events. *Atmos. Meas. Tech.* **17**, 5243–5259 (2024).
24. Yoshimura, K., Miyoshi, T. & Kanamitsu, M. Observation system simulation experiments using water vapor isotope information. *J. Geophys. Res. Atmos.* **119**, 7842–7862 (2014).
25. Tada, M., Yoshimura, K. & Toride, K. Improving weather forecasting by assimilation of water vapor isotopes. *Sci. Rep.* **11**, 18067 (2021).
26. Yoshimura, K. et al. Comparison of an isotopic atmospheric general circulation model with new quasi-global satellite measurements of water vapor isotopologues. *J. Geophys. Res.* **116**, D19118 (2011).
27. Risi, C. et al. Process-evaluation of tropospheric humidity simulated by general circulation models using water vapor isotopologues: 1. Comparison between models and observations. *J. Geophys. Res. Atmos*. **117**, D05304 (2012).
28. Bong, H. et al. Process-based intercomparison of water isotope-enabled models and reanalysis nudging effects. *J. Geophys. Res. Atmos*. **129**, e2023JD038719 (2024).
29. Yoshimura, K., Kanamitsu, M., Noone, D. & Oki, T. Historical isotope simulation using reanalysis atmospheric data. *J. Geophys. Res.* **113**, D19108 (2008).
30. Schneider, M., Yoshimura, K., Hase, F. & Blumenstock, T. The ground-based FTIR network's potential for investigating the atmospheric water cycle. *Atmos. Chem. Phys.* **10**, 3427–3442 (2010).
31. Hunt, B. R., Kostelich, E. J. & Szunyogh, I. Efficient data assimilation for spatiotemporal chaos: a local ensemble transform Kalman filter. *Phys. D Nonlinear Phenom.* **230**, 112–126 (2007).
32. Fisher, D. A. A zonally-averaged stable-isotope model coupled to a regional variable-elevation stable-isotope model. *Ann. Glaciol.* **14**, 65–71 (1990).
33. Rozanski, K., Araguás-Araguás, L. & Gonfiantini, R. Isotopic patterns in modern global precipitation in *Geophysical Monograph Series*, 1–36. https://doi.org/10.1029/GM078p0001 (1993).
34. Lee, J., Pierrehumbert, R., Swann, A. & Lintner, B. R. Sensitivity of stable water isotopic values to convective parameterization schemes. *Geophys. Res. Lett.* **36**, 1–5 (2009).
35. Risi, C. et al. Process-evaluation of tropospheric humidity simulated by general circulation models using water vapor isotopic observations: 2. Using isotopic diagnostics to understand the mid and upper tropospheric moist bias in the tropics and subtropics. *J. Geophys. Res. Atmos*. **117**, D05303 (2012).
36. Joussaume, S., Sadourny, R. & Jouzel, J. A general circulation model of water isotope cycles in the atmosphere. *Nature* **311**, 24–29 (1984).
37. Hoffmann, G., Werner, M. & Heimann, M. Water isotope module of the ECHAM atmospheric general circulation model: a study on timescales from days to several years. *J. Geophys. Res. Atmos.* **103**, 16871–16896 (1998).
38. Sturm, K., Hoffmann, G., Langmann, B. & Stichler, W. Simulation of $\delta^{18}O$ in precipitation by the regional circulation model REMOiso. *Hydrol. Process.* **19**, 3425–3444 (2005).

39. Schmidt, G. A., LeGrande, A. N. & Hoffmann, G. Water isotope expressions of intrinsic and forced variability in a coupled ocean-atmosphere model. *J. Geophys. Res. Atmos.* **112**, 1–18 (2007).
40. Risi, C., Bony, S., Vimeux, F. & Jouzel, J. Water-stable isotopes in the LMDZ4 general circulation model: model evaluation for present-day and past climates and applications to climatic interpretations of tropical isotopic records. *J. Geophys. Res.* **115**, D12118 (2010).
41. Diekmann, C. J. et al. A Lagrangian perspective on stable water isotopes during the West African monsoon. *J. Geophys. Res. Atmos.* **126**, 1–23 (2021).
42. Kang, J.-S. et al. "Variable localization" in an ensemble Kalman filter: application to the carbon cycle data assimilation. *J. Geophys. Res.* **116**, D09110 (2011).
43. Blossey, P. N., Kuang, Z. & Romps, D. M. Isotopic composition of water in the tropical tropopause layer in cloud-resolving simulations of an idealized tropical circulation. *J. Geophys. Res. Atmos.* **115**, 1–23 (2010).
44. Pfahl, S., Wernli, H. & Yoshimura, K. The isotopic composition of precipitation from a winter storm—a case study with the limited-area model COSMO iso. *Atmos. Chem. Phys.* **12**, 1629–1648 (2012).
45. Wei, Z., Lee, X. & Patton, E. G. ISOLESC: a coupled isotope-LSM-LES-cloud modeling system to investigate the water budget in the atmospheric boundary layer. *J. Adv. Model. Earth Syst.* **10**, 2589–2617 (2018).
46. Tanoue, M. et al. Modeling water isotopes using a global non-hydrostatic model with an explicit convection: comparison with gridded data sets and site observations. *J. Geophys. Res. Atmos.* **128**, 1–29 (2023).
47. Schneider, M. et al. Design and description of the MUSICA IASI full retrieval product. *Earth Syst. Sci. Data* **14**, 709–742 (2021).
48. Okazaki, A. & Yoshimura, K. Global evaluation of proxy system models for stable water isotopes with realistic atmospheric forcing. *J. Geophys. Res. Atmos.* **124**, 8972–8993 (2019).
49. Cauquoin, A. & Werner, M. High-resolution nudged isotope modeling with ECHAM6-Wiso: impacts of updated model physics and ERA5 reanalysis data. *J. Adv. Model. Earth Syst.* **13**, 1–19 (2021).
50. Yeo, N., Chang, E. & Yoshimura, K. Application of a semi-Lagrangian advection scheme for transport of stable water isotopes in the Isotope-incorporated Global Spectral Model (IsoGSM). *J. Geophys. Res. Atmos*. **130**, e2024JD043154 (2025).
51. Kanamitsu, M. et al. NCEP–DOE AMIP-II reanalysis (R-2). *Bull. Am. Meteorol. Soc.* **83**, 1631–1644 (2002).
52. Whitaker, J. S. & Hamill, T. M. Evaluating methods to account for system errors in ensemble data assimilation. *Mon. Weather Rev.* **140**, 3078–3089 (2012).
53. Hersbach, H. et al. The ERA5 global reanalysis. *Q. J. R. Meteorol. Soc.* **146**, 1999–2049 (2020).
54. Huffman, G. et al. *NASA GPM Integrated Multi-satellitE Retrievals for GPM (IMERG) Algorithm Theoretical Basis Document (ATBD) Version 06* (National Aeronautics and Space Administration, 2020).

## Acknowledgements
We thank V. Maithel and G. Bennett-Pierre at the Cooperative Institute for Research in Environmental Sciences for feedback on the paper. We thank the editor and reviewers for their valuable feedback.

## Author contributions
K.T., Y.K. and M.S. conceptualized the study. M.S., C.D., F.K. and B.E. created the IASI data. H.B. performed the nudging simulations. K.T. processed the raw datasets, performed the assimilation experiments, and analyzed the results. K.T., Y.K., M.S., C.D. and F.K. provided technical input and contributed ideas. K.T. and Y.K. wrote the original draft. All authors reviewed and edited the paper.

## Funding
This work was supported by JSPS KAKENHI Grant (21H05002; 22H04938), Japanese MEXT program (JPMXD0722680395), JST SICORP (JPMJSC22E4), JST Moonshot (JPMJMS2282-08), JST Mirai (JPMJMI24I1), MEXT ArCS2 (JPMXD1420318865), and ERCA S20 (JPMEERF21S12020). K.T. was supported by JSPS KAKENHI Grant (19J01337). M.S., C.D., F.K. and B.E. were supported by the Deutsche Forschungsgemeinschaft via the projects MOTIV (290612604) and TEDDY (416767181), the European Space Agency via the project Sentinel-5p +Innovation–Water Vapour Isotopologues (S5P+I–H2O-ISO), and the Helmholtz Association through Programme-Oriented Funding (PoF IV) within the research field Earth and Environment under the programme Changing Earth—Sustaining Our Future. An important part of this work was performed on the supercomputer HoreKa, funded by the Ministry of Science, Research and the Arts Baden-Württemberg and by the German Federal Ministry of Education and Research.

## Competing interests
The authors declare no competing interests.

## Additional information
**Supplementary information** The online version contains supplementary material available at https://doi.org/10.1038/s43247-026-03917-x.

**Correspondence** and requests for materials should be addressed to Kinya Toride.

**Peer review information** *Communications Earth & Environment* thanks Philipp Griewank and the other anonymous reviewer(s) for their contribution to the peer review of this work. Primary handling editors: Joe Aslin and Aliénor Lavergne. A peer review file is available.